Study on the recovery rate of natural hydrate particles in the protrusion of the mining chamber

Lin Zhong[1, 2,*], Wenchao Zhang[1,2], Dangfei Wang[1,2], Qing Feng[1,2]

[1]School of Mechanical and Electrical Engineering, Southwest Petroleum University, Sichuan, 610500 China

[2]Energy Equipment Institute, Southwest Petroleum University, Sichuan 610500, China.

*Corresponding author: zhonglin858296@163.com

Abstract

Solid-state fluidization is a new method for exploiting natural gas hydrate (NGH), and the recovery of natural gas hydrate particles in a mining chamber determines its mining efficiency. The recovery of hydrate particle was significantly impacted by circular protrusions that developed on the inside wall of the mining chamber after the water jet. In order to improve the particle recovery rate, this paper uses experimental and simulation methods to conduct research, we used to establish DDPM numerical model and accuracy of the numerical model is demonstrated by comparing simulation results with experiments. Finally, analyzing the impact of recovery hole spacing (l) and particle diameter (d_1) on particle recovery performance with the mining chamber's protrusion in solid-state fluidization mining for NGH. The outcomes demonstrate that when l is 100 mm and s is 60 mm, the recovery rate gradually decreases with the increase of protrusion height (h), but when is 20 mm, the recovery rate increases with the increase of protrusion spacing (s). When d1 is 0.5 mm, no matter how h or s are, the recovery rate is at its maximum. With the increase in particle diameter, as the increase in particle mass leads to the weakening of flow field uplift, the recovery rate will drop sharply.

Keywords

Solid-state fluidization, Recovery rate, mining chamber, Recovery hole spacing, Particle diameter.

1. Introduction

Natural gas hydrate (NGH) is an ice-like solid compound formed by methane and water molecules under high pressure and low temperature [1,2], which can release 164 times of natural gas per unit volume [3]. NGH is regarded as a promising clean alternative energy for the 21st century due to its high energy density and enormous reserves [4,5]. With an estimated total production of 6.5 to 10.5 billion cubic meters, China's NGH is primarily distributed in the South China Sea [6]. The special geological conditions and features of the South China Sea's NGH make mining them extremely difficult. Most of the gas hydrates are non-diagenetic hydrates with weak cementation, no stable cap rock, and shallow depths. Conventional mining techniques also have risks of reservoir collapse and submarine landslides, as well as risks related to face geology, equipment, and the environment [7,8,9,10].

To avoid potential risks, Zhou [11] proposed the solid-state fluidization mining method in 2014 for the NGH reservoir located in shallow layers of deep water. This method was successfully applied to the South China Sea trial exploration of NGH in 2017 [12]. As one of the core technologies of solid-state fluidization mining method, hydraulic suction has played a pivotal role in influencing the production of natural gas directly, as well as determining the efficiency

ISSN: 1813-4890

of the hydrate extraction process. Wang [13] studied the recovery tool parameters under single jetting and found that under the same total recovery port area, the suction impact of the small recovery port was superior to that of the large recovery port. Yang [14] used the numerical simulation method to study the particle transport law, and he found the hydraulic suction capacity is limited with single jetting and many particles migrate along the wall to the bottom. On the basis of single jet recovery, Yu [15] proposed a dual jet recovery scheme and studied the effect of front and rear jet spacing and particle properties on the particle recovery and migration of hydrate by means of experimentation and numerical simulation. However, above scholars regarded the mining chamber as a smooth wall and then conducted a study of hydrate recovery performance. In fact, there are protruding parts on the wall of the mining chamber after jet crushing, and the protruding wall of the mining chamber will affect the migration and recovery of particles. Wang [16] has conducted research on the influence of the protruding wall of the mining chamber on the particle recovery flow field and recovery rate, but he ignored the effects of the physical properties of particles and the spacing of recovery holes in actual mining.

In order to improve the investigation of the effect of the protrusion of the mining chamber on hydrate recovery performance. In this paper, the influence of factors such as particle property and hole spacing on the recovery rate in the mining cavity under the influence of the protrusion wall of the mining chamber parameters was studied in order to provide theoretical guidance for the design and process parameters of the actual hydrate particle recovery tools.

2. Experimental study

2.1. Experimental equipment

We have obtained the protrusion wall of the solid-state fluidization mining chamber parameter from the land well experiment, as shown in Fig. 1. We got the actual crushing chamber, then used a 3D scanner to scan the inner wall of the mining chamber and Geomagic Spark software to export images and data, as shown in Fig.2. Finally, we can get the protrusion feature parameters: a height (h) of 20 – 60 mm and a spacing (s) of 60 – 120 mm.

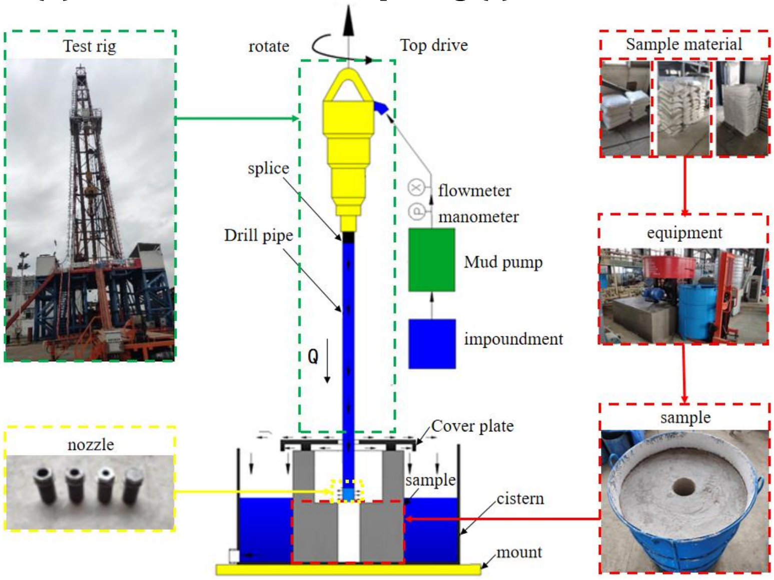

Fig.1 The diagram of Gas hydrate jet crushing test system

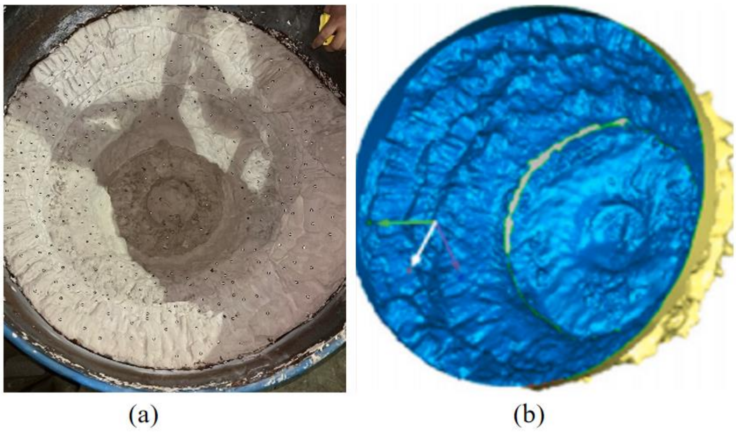

Fig.2 (a) The true shape in the mining chamber; (b) The shape of mining chamber after scanning

As shown in Fig. 3, the experimental setup includes a slurry preparation tank, valve, flow meter, and experimental box. As the real marine natural gas hydrate can only be stored in an environment of low temperature and high pressure, it is difficult to carry out experimental research on its crushing and recovery under laboratory conditions of normal temperature and pressure. We chose quartz sand (particle size 150 μm) as the experimental sample, because quartz sand and hydrate sediment particles are not very different in physical properties, small differences between the two are negligible in experiments.

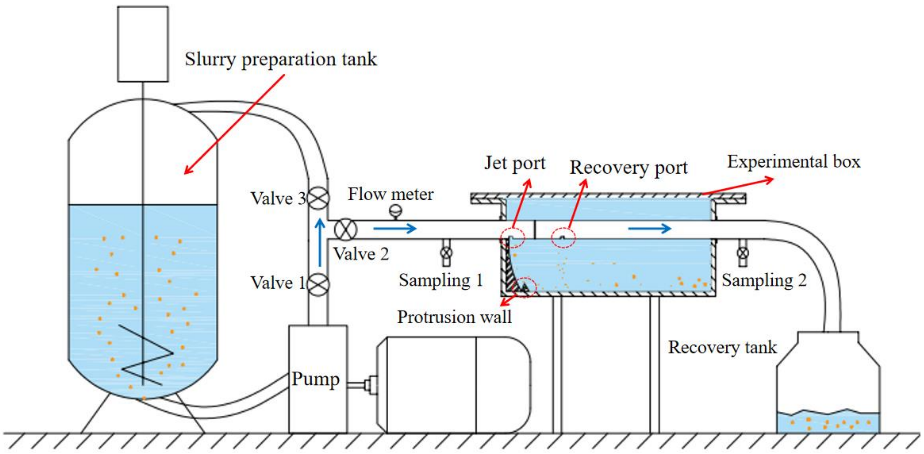

Fig. 3 The diagram of experimental setup

2.2 Experimental scheme

In this paper, the particle recovery rate (φ) is regarded as the research objective, which is defined as the ratio of inlet mass flow rate to outlet mass flow rate. Samples are taken at the inlet and outlet at the same time t, respectively. Then, volume measurement and weighing of samples are performed. The specific calculation method is as follows:

$$\dot{m}_1 = m_1 / t_1 \tag{1}$$

$$t_1 = V_1 / Q \tag{2}$$

$$\dot{m}_2 = m_2 / t_2 \tag{3}$$

$$t_2 = V_2 / Q \tag{4}$$

$$\varphi = \frac{\dot{m}_2}{\dot{m}_1} \times 100\% = \frac{m_2 V_1}{m_1 V_2} \times 100\% \tag{5}$$

where $\dot{m}_1$ is the inlet mass flow rate, m_1 is the sand mass of inlet, t_1 is the sampling time of inlet, V_1 is the sampling volume of inlet, Q is the flow rate of experiment, $\dot{m}_2$ is the outlet mass flow rate, t_2 is he sampling time of outlet, V_2 is the sampling volume of outlet.

The experimental process is that, firstly, we should prepare the evenly mixed slurry which according to a certain volume ratio of sand and water in the slurry preparation tank. Secondly, open the valves 1 and 2 to allow the slurry to circulate in the circuit, then the valve 3 was opened and the flow meter was adjusted to stabilize the flow rate at 10.2 m^3 /h. Finally, we take the samples at the sampling 1 and 2, then carried out 3 times in each experiment. The experimental parameters are shown in Table 1.

Table 1 Experimental parameters of NGH recovery with different protrusion height.

No.	Flow rate (m3/h)	h（mm）	s（mm）
1	10.2	0	80
2	10.2	10	80
3	10.2	20	80
4	10.2	30	80
5	10.2	40	80
6	10.2	50	80

3. Numerical study

3.1 Governing equation

The DDPM model is used for numerical calculation, in which the liquid phase is continuous phase and the solid particles are discrete phase. The turbulence model is modeled using the Realizable k-ε model, and the force between the liquid and solid phases is considered a virtual mass force and an additional force caused by the pressure gradient. The influence of the solid particles' size and shape was disregarded, and the solid particles were assumed to be uniformly spherical particles. The basic governing equation is as follows:

The continuity equation

$$\frac{\partial \rho}{\partial t}+\frac{\partial \rho u}{\partial x}+\frac{\partial \rho v}{\partial y}+\frac{\partial \rho w}{\partial z}=0 \tag{6}$$

Where, ρ is the density of fluid, kg/m^3; u, v, w is velocity component direction of the x, y, and z axes, m/s.

The momentum equation

$$\frac{\partial(\rho\bar{v})}{\partial t}+\nabla\cdot(\rho\bar{v})=-\nabla p+\nabla(\overset{=}{\tau})+\rho\vec{g} \tag{7}$$

$$\overset{=}{\tau}=\mu[(\nabla\bar{v})-\frac{2}{3}\nabla\cdot\bar{v}] \tag{8}$$

Where, $\bar{v}$ is three-dimensional velocity vector, kg/m^3; $\rho\vec{g}$ is gravity, N; $\overset{=}{\tau}$ is tensor of stress; μ is fluid viscosity, $Pa\cdot s$.

The equation of Realizable *k*-*ε* model

The Realizable *k*-*ε* model is based on the *Boussinesq* vortex viscosity hypothesis, so the relationship between Reynolds stress and the average velocity gradient is established as follows:

$$-\rho\overline{u_i^{'}}\overline{u_j^{'}}=\mu_t(\frac{\partial\bar{u}_i}{\partial x_j}+\frac{\partial\bar{u}_j}{\partial x_j})-\frac{2}{3}\rho k\delta_{ij} \tag{9}$$

Where μ_t is the turbulent viscosity; k is turbulent kinetic energy. Therefore, the transport equation for turbulent kinetic energy and turbulent kinetic energy dissipation rate in the standard model is as follows:

$$\frac{\partial}{\partial t}(\rho k)+\frac{\partial}{\partial x_i}(\rho k u_i)=\frac{\partial}{\partial x_j}[(\mu+\frac{\mu_t}{\sigma_k})\frac{\partial k}{\partial x_j}]+G_k+G_b-\rho\varepsilon-Y_M+S_k \tag{10}$$

$$\frac{\partial}{\partial t}(\rho \varepsilon)+\frac{\partial}{\partial x_i}(\rho \varepsilon u_i)=\frac{\partial}{\partial x_i}[(\mu+\frac{\mu_t}{\sigma_\varepsilon})\frac{\partial \varepsilon}{\partial x_j}]+C_{1\varepsilon}\frac{\varepsilon}{k}(G_k+C_{3\varepsilon}G_b)-C_{2\varepsilon}\rho\frac{\varepsilon^2}{k}+S_\varepsilon \tag{11}$$

Where, G_k is the generation of turbulence kinetic energy due to the average velocity gradients, G_b is the generation of turbulence kinetic energy due to buoyancy, Y_M is the contribution of the fluctuating dilatation in compressible turbulence to the overall dissipation rate, $C_{1\varepsilon}$, $C_{2\varepsilon}$, and $C_{3\varepsilon}$ are constants. σ_k and σ_ε are the turbulent Prandtl numbers for k and ε, respectively. S_k and S_ε are user-defined source terms.

$$G_k=-\rho\overline{u_i^{'}}\overline{u_j^{'}}\frac{\partial u_j}{\partial x_i} \tag{12}$$

$$\mu_t=\rho C_\mu\frac{k^2}{\varepsilon} \tag{13}$$

The value of the constant is: $C_{1\varepsilon}$ = 1.44, $C_{2\varepsilon}$ = 1.92, C_μ = 0.09, σ_k = 1.0, σ_ε = 1.3.

The equation of particle motion

In this paper, the dense particle flow model DDPM in the particle analysis method based on the Euler-Lagrange method is mainly used. In the standard formula of the discrete phase model, the volume fraction of the discrete phase is assumed to be low enough. The general form of mass and momentum conservation equations in ANSYS Fluent is:

$$\frac{\partial\rho}{\partial t}+\nabla\cdot(\rho\vec{v})=S_{DPM}+S_{other} \tag{14}$$

$$\frac{\partial\rho\vec{v}}{\partial t}+\nabla\cdot(\rho\vec{v}\vec{v})=-\nabla p+\nabla\tau+\rho\vec{g}+\vec{F}_{DPM}+\vec{F}_{other} \tag{15}$$

$$\frac{\partial}{\partial t}(\alpha_p\rho_p)+\nabla\cdot(\alpha_p\rho_p\vec{v}_p)=\sum_{q=1}^{nphase}(\dot{m}_{qp}-\dot{m}_{pq}) \tag{16}$$

Due to the high content of solid particles in the process of natural gas hydration, the interaction between particles and the interaction between particles and fluids cannot be ignored. Therefore, in order to overcome the limitations of the discrete phase hypothesis, the dense particle flow model extends the mass conservation equation and the momentum conservation equation to calculate the volume fraction of the discrete phase:

$$\begin{aligned}&\frac{\partial}{\partial t}(\alpha_p\rho_p\vec{v}_p)+\nabla(\alpha_p\rho_p\vec{v}_p\vec{v}_p)=\\&-\alpha_p\nabla p+\nabla\cdot[\alpha_p u_p(\nabla\vec{v}_p+\nabla\vec{v}_p^T)]+\alpha_p\rho_p\vec{g}+F_{vm,lift,user}+\\&\sum_{q=1}^{nphase}(\vec{K}_{qp}(\vec{v}_q-\vec{v}_p)+\dot{m}_{qp}\vec{v}_{qp}-\dot{m}_{pq}\vec{v}_{pq})+K_{DPM}(\vec{v}_{DPM}-\vec{v}_p)+S_{DPM,\text{explicit}}\end{aligned} \tag{17}$$

Where, S_{DPM} is the particle averaged velocity; K_{DPM} is particle averaged interphase momentum exchange coefficient.

3.2 Geometric model

Because of gravitational acceleration, the trajectory of particles in the mining chamber is non-axisymmetric, so we used a three-dimensional model to simulate the process of hydrate particles recovery. A symmetry plane is set along the direction of gravity, and the fluid region is simplified into a semi-cylinder. At the same time, simplify the jet nozzle and recovery port into 5 mm and 15 mm circumferential belts of the tool. The structure is shown in Fig. 4, and the structural parameters are shown in Table 2.

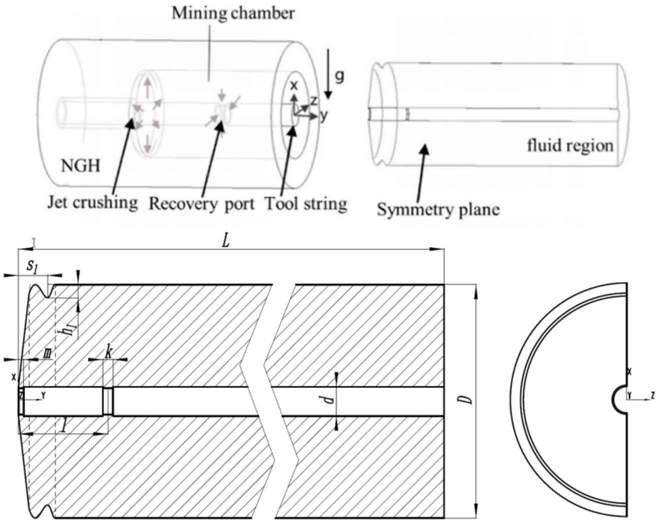

Fig.4 Schematic diagram of model structure

Table 2 Structural parameters of the model.

Parameters	Symbol	Value
Model length (mm)	L	2000
Jet nozzle size (mm)	m	5
Recovery hole size (mm)	k	15
Recovery hole spacing(mm)	l	300~900
Protrusion height (mm)	h	20
Protrusion spacing (mm)	s	60
particle diameter (mm)	d1	0.1~5
Mining chamber diameter (mm)	D	800
Tool string diameter (mm)	d	100

3.3 Grid division and model verification

With Fluent-meshing software, the calculation domain of NGH recovery was divided with an unstructured grid. In order to ensure the grid independence of the simulations, six kinds of grids with 107973, 255797, 377701, 530343, 608927, and 988559 cells, then we verify these six grids. The particle recovery rate of the simulation results was compared, as shown in Fig. 5. It can be seen that when the number of grids is more than 530000, the change in particle recovery rate is very slight. Therefore, we consider the calculation accuracy and time, so the calculation domain is divided into 530,343 units.

In order to verify the correctness of the model, we compare the simulation results with the experimental results, as shown in Fig.6. We can see from the figure that the error between the two is less than 10%, indicating that the model can simulate the experiment correctly.

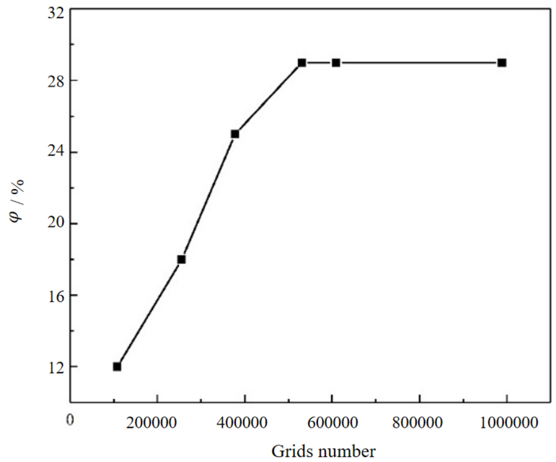

Fig.5 Comparison of the particle recovery rates at different grids number.

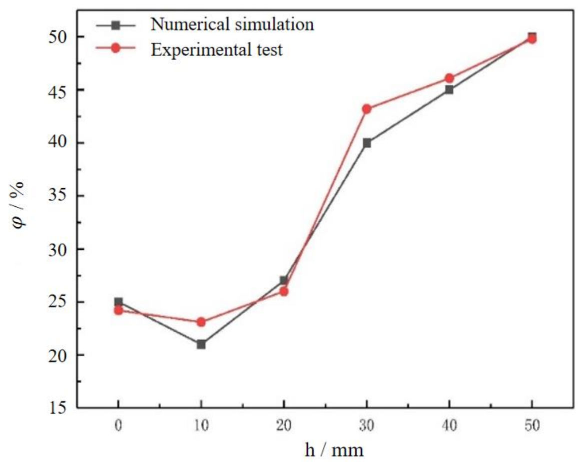

Fig.6 Comparison of the particle recovery rates between experimental tests and numerical simulations.

4. Results and discussion

4.1 Effect of the distance between the recovery ports

Fig. 7 indicates the relationship between the particle recovery rate and recovery hole spacing with various protrusion height. When s = 60 mm, no matter how h is, with an increase in l, the particle recovery rate swings up and down and finally drops substantially before fluctuating around 10 %. When l = 100 mm, the recovery rate of the three h cases is at its maximum, and the recovery rate has dropped markedly with an increase in h.

According to the results of Wang's study on the flow field characteristics of protrusion height and protrusion spacing [16], we can inference that this is because the lower portion of the flow field cannot be elevated when s = 60 mm, making it difficult to recovery hydrate particles. However, when h = 40 and 60 mm, there is an inflection point where the recovery rate suddenly increases which maximum is about 59 %, mainly because the flow field changes and the upper and lower fields strengthen to promote the recovery of particles.

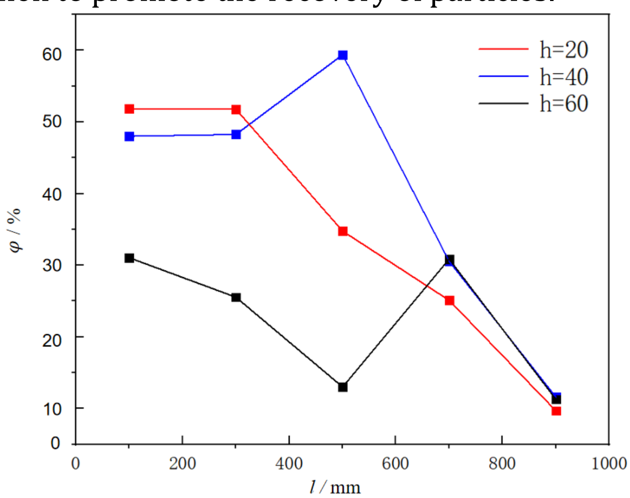

Fig.7 Variation of particle recovery rate with recovery hole spacing at different protrusion height.

Fig. 8 indicates the relationship between the particle recovery rate and recovery hole spacing with various protrusion spacing. When h = 20 mm, the change trend of the curve in the figure is similar to that in Fig. 8, but the final recovery rate is about 20 %. When l = 100 mm, the recovery rate is at its maximum value, which fluctuates up and down with the increase of l but still decreases continuously. But when l = 100 mm, with an increase in s, the recovery rate is increase.

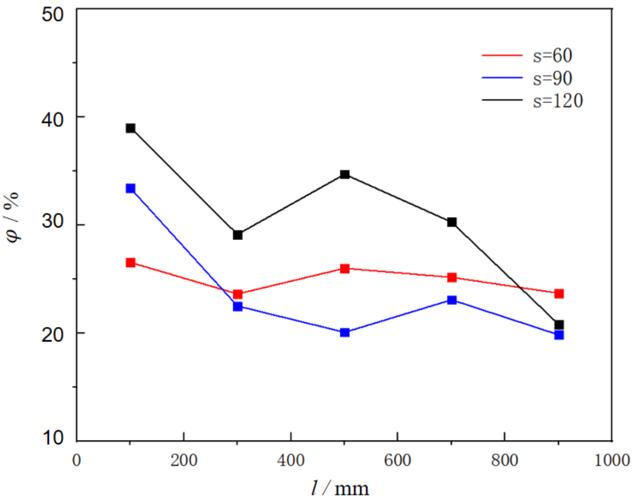

Fig.8 Variation of particle recovery rate with recovery hole spacing at different protrusion spacing.

4.2 Effect of particle size on recovery rate

Fig. 9 and Fig. 10 indicates the relationship between the particle recovery rate and particle diameter with various protrusion height and protrusion spacing. When the d_1 is less than 0.5 mm, the recovery rate shows an upward trend, mainly because the particle size is small, the weight is light, and it is easy to be lifted by the flow field, which leads to an improvement in the recovery rate. With the increase in particle diameter (d_1 > 0.5mm), the uplift of the flow field becomes weaker, and the recovery rate drops sharply.

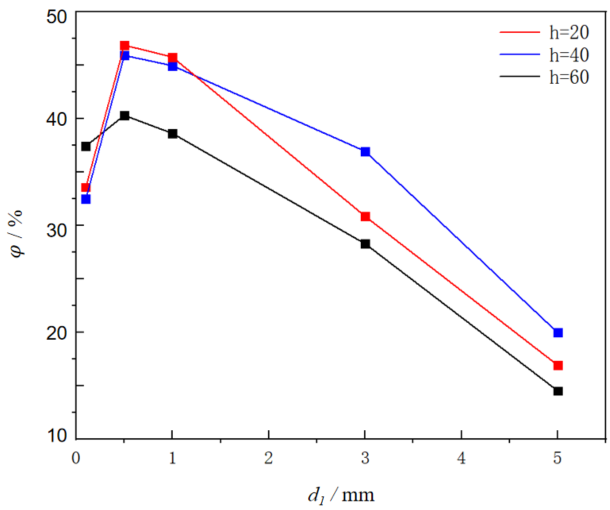

Fig.10 Variation of particle recovery rate with particle diameter at different protrusion height.

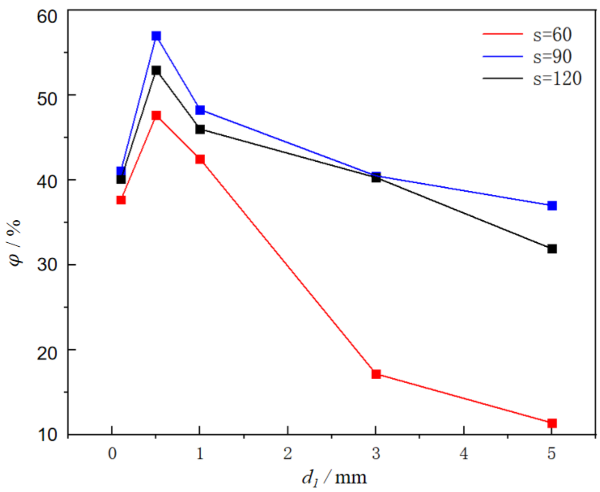

Fig.11 Variation of particle recovery rate with particle diameter at different protrusion spacing.

5. Conclusion

In this paper, we adopt the research method of combining experiment and simulation. The accuracy of the numerical model is demonstrated by comparing simulation results with experiments, then analyzing the impact of recovery hole spacing and particle diameter on particle recovery performance with the mining chamber's protrusion in solid-state fluidization mining for NGH. The results of this study lead to the following conclusions:

When s = 60 mm, no matter how h is, due to lower portion of the flow field cannot be elevated, so with an increase in l, the recovery rate will drop about 10 %. When h = 20 mm, no matter how s is, with an increase in l, the final recovery rate is about 20 %. But when h = 40 and 60 mm, the recovery rate will have an inflection point which the recovery rate will increase, this because the flow field changes and the upper and lower fields strengthen to promote the recovery of particles.

When l = 100 mm and s = 60mm, the recovery rate gradually decreases with the increase of h, but when h is fixed and does not change to 20mm, the recovery rate increases with the increase of s.

When d_1 = 0.5mm, no matter how h or s are, the recovery rate is at its maximum. With the increase in particle diameter, as the increase in particle mass leads to the weakening of flow field uplift, the recovery rate will drop sharply.

Acknowledgements

We would like to express our thanks for the sponsorship of National Key Research and Development Program of China (2019YFC0312305), National Natural Science Foundation project of China (52374011), Strategic Consulting Project of Chinese Academy of Engineering (2022XBZD0803) and Sichuan Science and Technology Program (2023NSFSC1980).

References

[1] A. Kumar, H.P. Veluswamy, et al. Molecular level investigations and stability analysis of mixed methane-tetrahydrofuran hydrates: implications to energy storage, Fuel, Vol. 236 (2019), p.1505–1511.

[2] M.J. Yang, Z. Fu, Y.C. Zhao, et al. Effect of depressurization pressure on methane recovery from hydrate–gas–water bearing sediments, Fuel, Vol. 166 (2016), p. 419–426.

[3] K.A. Kvenvolden: Gas hydrates - geological perspective and global change. Reviews Geophysics, Vol. 31 (1993) No. 2, p.173–187.

[4] H.R. Sun, B.B. Chen, et al. Utilization of water-gas flow on natural gas hydrate recovery with different depressurization modes, Fuel, Vol. 288 (2021).

[5] P.F. Wang, M.J. Yang, et al. Methane hydrate reformation in porous media with methane migration, Chemical Engineering Science, Vol. 168 (2017), p.344–351.

[6] Y. Song, L. Yang, et al. The status of natural gas hydrate research in China: A review, Renewable & Sustainable Energy Reviews, Vol. 31 (2014), p.778-791.

[7] X. Li, C. Xu., Y. Zhang, et al. Investigation into gas production from natural gas hydrate: A review, Applied Energy, Vol. 172 (2016.), p.286-322.

[8] J. He, Q. Liang., Y. Ma., et al. Geohazards types and their distribution characteristics in the natural gas hydrate area on the northern slope of the South China Sea, Geology in China, Vol. 45 (2018) No. 1, p.15-28.

[9] Malagar, R.C. Bhini, K.P. Lijith: Formation & dissociation of methane gas hydrates in sediments: A critical review. Journal of Natural Gas Science & Engineering, Vol. 65 (2019), p.168-184.

[10] F. Ning, J. Liang, N. Wu, et al. Reservoir characteristics of natural gas hydrates in China, Natural Gas Industry, Vol. 40 (2020) No. 8, p.1-24.

[11] S.W. Zhou, W. Chen, Q.P. Li: The green solid fluidization development principle of natural gas hydrate stored in shallow layers of deep water, China Offshore Oil Gas, Vol. 26 (2014), p.1-7.

[12] S.W. Zhou, W. Chen, Q.P. Li, et al. Research on the Solid Fluidization Well Testing and Production for Shallow Non-Diagenetic Natural Gas Hydrate in Deep Water Area, China Offshore Oil and Gas, Vol. 29 (2017), No. 4, p.1-8.

[13] G.S. Wang: Research on solid-liquid two-phase flow in shallow water hydrate fragmentation and ore collection recovery (MS., SouthWest Petroleum University, China 2019), p.31.

[14] P. Yang, G.R. Wang: Numerical simulation of transportation of particles in jet breaking with solid fluidization method, Shipbuilding of China, Vol. 60 (2019) No. 4, p.108-114.

[15] X.Y. Yu: Study on the movement of mineral particles recovered from double-jet solid fluid hydrate slurry (MS., SouthWest Petroleum University, China 2022), p.27.

[16] D.F. Wang, G.R. Wang, L. Zhong: Effect of the protrusion of the mining chamber on particle recovery performance in solid-state fluidization mining for natural gas hydrate, Geoenergy Science and Engineering, Vol. 233 (2024).